Title

Drug-drug conjugates self-assembled nanomedicines triggered photo-/immuno- therapy for synergistic cancer treatments.

Authors

Qu, Haijing

Li, Longmeng

Chen, Han

et al.

Publication Date

2023-11-01

DOI

10.1016/j.jconrel.2023.09.042

Peer reviewed

HHS Public Access

Author manuscript

J Control Release. Author manuscript; available in PMC 2024 November 01.

Published in final edited form as:

J Control Release. 2023 November ; 363: 361–375. doi:10.1016/j.jconrel.2023.09.042.

Drug-drug conjugates self-assembled nanomedicines triggered photo-/immuno- therapy for synergistic cancer treatments

Haijing Qu[a,b,1], **Longmeng Li**[c,1], **Han Chen**[a,b], **Menghuan Tang**[c], **Wei Cheng**[a,b], **Tzu-yin Lin**[d], **Lingyan Li**[e], **Bin Li**[e,*], **Xiangdong Xue**[a,b,*]

[a.]Shanghai Frontiers Science Center of Drug Target Identification and Delivery, School of Pharmacy, Shanghai Jiao Tong University, Shanghai 200240, China.

[b.]National Key Laboratory of Innovative Immunotherapy, Shanghai Jiao Tong University, Shanghai 200240, China.

[c.]Department of Biochemistry and Molecular Medicine, UC Davis Comprehensive Cancer Center, University of California Davis, Sacramento, CA 95817, USA

[d.]Division of Hematology/Oncology, Department of Internal Medicine, University of California Davis, Sacramento, CA 95817, USA

[e.]Alphacait AI Biotech ch., LTD, No.10, Xixi Wetland, Wuchang Ave, Hangzhou, Zhejiang, 310023, China

Abstract

Although immunotherapies have made progress in cancer treatment, their clinical response rates vary widely and are typically low due to sparse immune cell infiltration (immune "cold") and suppressive tumor immune microenvironment (TIME). A simple yet effective approach that integrates a variety of immune-stimulating and TIME-modulating functions could potentially address this clinical challenge. Herein, we conjugate two small molecules, including a photosensitizer (pyropheophorbide-a, PA) and a Toll-like receptor 7/8 agonist (resiquimod, R848), into prodrug (PA-R848) that self-assembles into PA-R848 esterase responsive nanoparticles (PARE NPs) with 100% drug composition and synergistic photo-/immune- therapeutic effects. In PARE NPs, PA exhibits strong phototherapeutic effects which ablate the primary tumor directly and elicits immunogenic cell death (ICD) to promote the immune response. R848 effectively polarizes the M2-type tumor-associated macrophage (TAM) to M1-type TAM, consequently reversing the “cold” and suppressive TIME when working together with phototherapy. The PARE NPs can efficiently pare down the tumor development by two synergisms, including i) synergistic immunotherapy between ICD and TAM polarization; ii) and the antitumor effects between phototherapy and immunotherapy. On a head-neck squamous cell carcinoma mouse model, PARE NPs combined with PD-1 antibody eliminate primary tumors, and significantly inhibit the progress of distant tumors thanks to the robust antitumor immunity enhanced by the PARE NPs.

*Corresponding authors: X. Xue, xuexd@sjtu.edu.cn; B. Li, binli@alphacait.com.

[1]H. Qu and L. Li contributed equally to this work.

Competing interests

There is no competing to declare.

Keywords

Nanomedicine; phototherapy; immunotherapy; immune responses

1. Introduction

Immunotherapy holds great promise to improve cancer treatments. In contrast to conventional surgery, chemotherapy and radiotherapy in clinics, immunotherapy not only inhibits the progression of primary tumor, but also activates the anti-tumor immunity to spot metastatic tumors [1-3]. Although immunotherapy is promising, its response rates vary significantly across tumor types and are generally low due to sparse immune cell infiltration and suppressive tumor immune microenvironment (TIME). Multiple immune-negative cells, including myeloid-derived suppressive cells, tumor-associated macrophages (TAMs), regulatory T cells (Tregs), and tumor-associated dendritic cells, accommodate tumor development to create an immunosuppressive TIME [4, 5]. Among these immunosuppressive cells, TAMs account for 30~50% of the tumor mass. As a result, targeting TAMs may offer a powerful approach to cancer immunotherapy. TAMs are highly plastic and can be polarized into two opposing phenotypes: the M2-subtype, which is associated with tumor-supportiveness, and the M1 subtype, associated with inflammatory responses and tumoricidal activities. M2-TAMs can promote tumor development and metastasis by inhibiting the activation of CD8+ cytotoxic T lymphocytes (CTL) [6, 7]. Interestingly, M2-TAM can be polarized into its M1-type under particular stimulation, which would reverse the immunosuppressive TIME and prolong patient survival [8-11]. Toll-like receptor (TLR) is widely expressed in the innate immune cells (e.g., TAM and dendritic cell, DC) and plays a significant role in polarizing the TAM from M2 and M1 subtypes [12, 13]. Additionally, TLR contributes to DC recruitment and maturation, and subsequently stimulates the relevant cells to secrete proinflammatory cytokines for CTL activation [14, 15]. Immunotherapy based on immune checkpoint blockade (ICB) has received greater attention recently and is acknowledged as a revolutionary immunotherapeutic advancement for cancer treatment. By enlisting and activating CTL to target tumor cells, ICBs (such as anti-PD-1/PDL-1 and anti-CTLA) positively influence TIME [16-18]. However, due to insufficient immune responses that are unable to draw enough lymphocytes into tumor tissues, immunotherapy could only benefit a maximum of 30% of patients, yielding an unsatisfactory level of therapeutic effectiveness overall. Additionally, immune-related adverse effects are another hurdle for clinical application [16, 17, 19]. Hence, there is an urgent need to develop more effective combinational anti-cancer approaches.

Phototherapy, which has been extensively investigated as a potential cancer treatment method, directly obliterates tumor tissues by converting light energy to hyperthermia or reactive oxygen species (ROS) [20, 21]. However, phototherapy can only treat surface or local tumor lesions due to the limited light penetration; it will be ineffective for phototherapy to treat tumors buried in the depths of the body or for metastasis that has spread to a greater distance [22]. Combining phototherapy with other therapeutic modalities (e.g., immunotherapy) that can reach distant tumors for a synergistic effect would compensate for phototherapy's shortcomings [23]. Phototherapy could activate immunogenic

cell death (ICD), which creates tumor-associated antigens (TAA) from tumor cell residues, and hence galvanize systematic immune responses and promote anticancer efficacy. It has been extensively reported that nano-enabled phototherapy works synergistically with immunotherapy to improve the anti-tumor effect substantially [24, 25]. The synergistic photo-immunotherapy mediated by TLR7 agonist (R837) and photosensitizer (Indocyanine green, ICG) elicited robust immune responses and efficiently inhibited tumor growth in mouse models [26-28]. These developed photo-immunotherapeutics, however, require sophisticated chemical synthesis and show low drug-loading capacity. It has been reported that TLR7 agonist (e.g., R837) and TLR 7/8 dual-agonist (e.g., R848) showed high potency in promoting anti-tumor immunities. In comparison, R848 is more effective and has better water solubility than R837 [29]. Furthermore, R848 possesses greater involvement in driving DC maturation and TAM polarization from M2 to M1 [13, 30]. However, the limited water solubility of phototherapeutics and TLR agonists hinders their bioapplications, and the discrepancies in pharmacokinetics and physiochemical properties restrict the potentially synergistic combinations. By taking advantage of sophisticated nanotechnology, nanomedicine can transport water-insoluble therapeutics to improve their bioavailability, carry different therapeutics to synergistically integrate multiple therapies, and utilize altered vasculature and impaired lymphatic drainage to target tumors [31, 32]. To this point, nanomedicine has been shown to advance cancer immunotherapy in significant ways [33]. However, currently developed nanomedicines employ large proportions of excipients (generally more than 85%) as carriers, which extensively increases the R&D and biosafety evaluation of the nanomedicines. In our previous research, we developed various small molecule nanomedicines (SMNs) by directly assembling drug-drug pairs [22, 34, 35] or drug-drug conjugates [36-39] into nanostructures that involved very few or no excipients. Cui lab conjugated functional peptides and drugs to assemble them into nanoparticles, and in this way, they developed a series of one-component nanomedicines (OCNs) [40-42]. Similarly, the OCNs and SMNs both aim to eliminate or reduce excipient use, which could significantly simplify the manufacturing procedures, improve delivery efficiency and increase the biosafety of the nanomedicines. To pursue the above-mentioned advantages, we intend to combine tumor-ablating phototherapy with TLR7/8 agonists by employing the simple yet effective SMN strategy to treat both primary and metastatic tumors.

In this study, a photosensitizer (Pyropheophorbide-a, PA) and TLR7/8 agonist (R848) were directly esterified to generate a prodrug (PA-R848), and further assembled into a PA-R848 esterase-responsive nanoparticles (PARE NPs) with 100% drug loading and synergistic photo-/immune- therapeutic effects (Scheme 1). The synergistic strategy based on PARE NPs could directly ablate primary tumor by phototherapy and inhibit distant tumor by phototherapy-promoted immunotherapy. In detail, phototherapy initially ablates the primary tumor upon laser irradiation, which could induce immunogenic cell death (ICD, #1), produce abundant TAAs (#2), and subsequently activate antigen-presenting cells (APC, such as DC) with R848. DCs that have reached maturity further process TAAs and present them to T cells in lymph nodes (#3), resulting in the recruitment and activation of CTL (#4), which then eliminates the primary tumor (#5) with the assistance of the ICB (#6). The R848 would be released to TIME and polarize the M2-like TAMs to the M1 type (#7), further promote the anti-tumoral immune response, and increase the killing

capacity of CTL against tumor cells by activating TLR. Activated T cells will continue to circulate and recognize metastatic tumor lesions as a result of the immunotherapy's abscopal effect (#8). In PARE NPs, phototherapy is capable of producing TAA, directly ablating the tumor mass, augmenting the systemic immune response, and synergizing the R848-mediated immunotherapy.

2. Materials and Methods

2.1. Materials and Reagents

Pyropheophorbide-a (PA) was purchased from Santa Cruz Biotechnology Inc. R848 was bought from Med Chem Express (MCE, USA). N, N'-Dicyclohexylcarbodiimide (DCC), 4-(Dimethylamino) pyridine (DMAP) and 2',70'-Dichlorofluorescin diacetate (DCF-DA) were from Sigma-Aldrich (MO, USA). All organic solvents were purchased from commercial resources and used directly without any purification. Milli-Q water (18.2 MΩ cm) was produced with a Milli-Q gradient system (Billerica, MA, USA). Lysotracker™ Green DND-26, Hoechst 33342 and DiD were purchased from Thermo Fisher Scientific Inc. Cell cultures medium, fetal bovine serum, cell cultures dishes and plates were purchased from Corning Inc.

2.2. Synthesis and characterization of PA-R848 prodrug

Firstly, the amine group of R848 was protected to avoid forming amine bond with PA. In detail, 4-amino-2-(ethoxymethyl)-α,α-dimethyl-1H-imidazo[4,5-c]quinoline-1-ethanol (R848, 3.0 g, 9.54 mmol) was added into 21 mL toluene to give a white suspension. Then, 1,4-diazabicyclo[2.2.2]octane (3.21 g, 28.6 mmol) and phtaloyl chloride (1.65 mL, 11.5 mmol) were added to the suspension and vigorously stirred at 110 °C for 4 h. The reaction system was diluted with 300 mL ethyl acetate and washed with 1 N hydrochloric acid after cooling to room temperature. The organic layers were collected and dried with $MgSO_4$, then filtered and concentrated by using a rotary evaporator. The amino-protected R848 was purified by column chromatography.

PA-R848 prodrug was synthesized by directly attaching protected R848 and PA via esterification. In detail, PA (534.65 mg, 1 mmol), DCC (412.6 mg, 2 mmol) and DMAP (30.55 mg, 0.25 mmol) were dissolved in 10 mL anhydrous chloroform, the mixture was stirred in an ice bath for 30 min. Then, protected R848 (222.09 mg, 0.5 mmol) was added into the reaction system and stirred in dark for another 24 h at room temperature. The reaction mixture was concentrated by a rotary evaporator. Then, the deprotection of R848 was then carried out. PA-R848 prodrug (protected) was dissolved in THF with hydrazine hydrate, the mixture was stirred for 2 h at room temperature prior to being cooled in an ice bath. DCM was used to extract the reaction system from 1 N hydrochloric acid. The organic layer was filtered and column chromatography was utilized to obtain PA-R848 prodrug. The successful synthesis of the prodrug was confirmed by MS, NMR spectrum and TLC traces.

2.3. Hemolysis evaluation of PA-R848 prodrugs

The hemolysis evaluation of PA-R848 prodrugs was carried out. In detail, red blood cells (RBCs) were collected from healthy BALB/c mice and washed twice

with PBS to remove the plasma, then diluted 10 times with PBS. The obtained RBCs were incubated with different concentrations of PA-R848 prodrugs for 1 h at 37 °C, the hemolysis condition of Triton X-100 (0.1%, vol/vol) was employed as a positive control (100%), PBS was a negative control, the hemolysis ratio was measured according to the absorbance at 540 nm via a microplate reader. To avoid PA-R848 prodrugs from forming PARE NPs, we directly added their DMSO solution (50 mM) into the RBC samples. The hemolysis ratio was calculated as follows: $\text{The hemolysis ratio} = (OD_{\text{sample}} - OD_{\text{negative control}}) / (OD_{\text{positive control}} - OD_{\text{negative control}}) \times 100\,\%$.

2.4. Cytotoxicity of PA-R848 prodrugs

The cytotoxicity of PA-R848 prodrugs was investigated by incubating with SCC-7 cells. In detail, the SCC-7 cells were seeded in 96-well plates overnight with a density of 5×10^3 cells per well. Then, the cells were incubated with different concentrations of PA-R848 prodrugs for 24 h. The medium was washed off and replaced with fresh medium. The laser-treated groups were exposed to 680 nm laser for 3 min, and further raised for another 24 h. The cell viability was measured by MTS Assay Kit according to the OD value at 490 nm.

2.5. Fabrication and characterization of PARE NPs

The PARE NPs were self-assembled via the re-precipitation method. In detail, 2 μL stock solution (50 mM in DMSO) of PA-R848 prodrugs was dropped into 998 μL Milli-Q water under sonication. Followed with 5 s vortex, 100 μM PARE NPs were fabricated. The particle size and polydispersity index (PDI) were measured by Malvern ZetaSizer nano ZS90 (Malvern Instruments, UK). The morphology of PARE NPs was observed by transmission electron microscopy (TEM, Philips CM-120) with 80 kV acceleration voltage. To prepare TEM sample, the aqueous suspension of PARE NPs was dropped onto copper grids and dried under ambient temperature. The optical behaviors of PARE NPs were measured with a UV–vis spectrometer (UV-1800, Shimadzu) and fluorescence spectrophotometer (RF-6000, Shimadzu), respectively. The stability of PARE NPs was investigated by monitoring the particle size and zeta potential with a ZetaSizer for 14 consecutive days.

2.6. Critical aggregation concentrations (CAC) of PARE NPs

CAC of PARE NPs was evaluated according to the pyrene ratiometric method. In detail, 1 μL of 0.1 mM pyrene solution (in acetone) was added to 999 μL PARE NPs at different concentrations, and incubated at 37 °C for 2 h. Thereafter, the fluorescence of pyrene was tested by using a fluorescence spectrophotometer (excitation is 335 nm). The I_3/I_1 values of pyrene against concentrations of PARE NPs were employed for CAC analysis.

2.7. ROS production and photothermal evaluation of PARE NPs

The ROS production profile of PARE NPs was measured by using SOSG. In detail, different concentrations of PARE NPs suspension were incubated with SOSG (10 μm) for 30 min, then exposed to 680 nm laser (0.5 w/cm^2) for 3 min. The fluorescence of SOSG was measured to indicate ROS production. For photothermal evaluation, different concentrations

of PARE NPs were exposed under 680 nm laser (0.5 w/cm^2) for 3 min. The temperature changes were recorded by a FLIR thermal camera.

2.8. Drug-releasing profile of PARE NPs stimulated by esterase

The drug-releasing profile of PARE NPs was evaluated by using esterase as stimulation. In detail, 200 μM PARE NPs were loaded into the dialysis cartridges (MWCO = 3.5 kDa) and immersed in 200 mL of phosphate buffer solution (PBS, pH 7.4). Esterase (100 U/mL) was added to the dialysis system to evaluate the responsive release. The dialysis system was placed in a 37 °C incubator under moderate stirring. The samples outside the dialysis cartridges were collected at different time intervals, and the concentrations of R848 were determined by HPLC (LC-20, Shimadzu) to give the accumulative drug-releasing profile (n=3). A SunFire C18 analytical column (150 mm, 4.6 mm, 5 μm, Waters) was employed to analyze the R848 at 25 °C with a gradient flow of mobile phase of solvent A (Milli-Q water with 0.1% formic acid) and solvent B (acetonitrile with 0.1% formic acid). The gradient phase (based on solvent A) was changed from 95% to 5% in 15 min. The flow speed was set to 1.0 mL/min. The absorbance of the UV–vis detector was set at 254 nm.

2.9. Cell culture

Cells were cultured in the indicated medium with 10% FBS and 1% antibiotics containing penicillin and streptomycin at 37 °C, 10% humidity and 5% CO_2 incubator. The murine HNSCC cells (SCC-7) and dendritic cells (DC 2.4), generously provided by Dr. Kit S. Lam's laboratory at UC Davis and routinely screened for mycoplasma, were cultured in DMEM and RPMI 1640 medium, respectively. Cell line authentication was performed by short tandem repeat DNA profiling. Murine bone-marrow-derived macrophages (BMDMs) used in morphological and polarization assays were isolated and derived according to the reference [12]. Bone marrow was extracted from femur and tibia of C57BL/6 mice, dissociated and passed through a 40 μm strainer, and red blood cells were lysed by ammonium chloride (StemCell Tech). Resultant bone marrow cells were cultured in 6 well plate in Iscove's DMEM supplemented with 10% FBS, 1% antibiotics containing penicillin and streptomycin and 20 ng/mL recombinant murine M-CSF (PeproTech, 315-02), the medium was replenished every two days.

2.10. Cytotoxicity of PARE NPs

The photo-cytotoxicity of PARE NPs on SCC-7 cells was further evaluated, the cells were treated with different concentrations of PA, R848, free PA/R848 mixture and PARE NPs for 24 h. The medium was washed off and replaced with fresh medium. The laser-treated groups were exposed to 680 nm laser for 3 min, and further raised for another 24 h. The cell viability was measured by MTS Assay Kit according to the OD value at 490 nm.

2.11. Cell distribution of PARE NPs

SCC-7 cells were seeded in 4-well microscopy chambers overnight with a density of 4×10^4 cells per well. After fully attached, the cells were treated with 10 μM PARE NPs for 2, 4 and 6 h, respectively. Then, the medium was removed and washed with PBS; the nuclei and lysosome stained with Hoechst 33342 (2 μg/mL, Thermo Scientific) and Lysotracker Green

for 10 min, respectively. The cell distributions of the PARE NPs and control materials were observed by confocal laser scanning microscopy (CLSM).

2.12. Intracellular ROS production and phototherapeutic effect of PARE NPs

SCC-7 cells were seeded in 6-well plates with 4×10^4 cells per well, and cultured overnight until completely attached. The cells were treated with 10 μM PARE NPs for 4 h, then exposed under laser irradiation for 3 min. After that, the cells were stained with DCFH-DA (10 μM) for 40 min, the DCF signal was measured by a microplate reader. For the phototherapeutic effect, SCC-7 cells were seeded in 4-well chamber slide with 4×10^4 cells per well, and cultured overnight until fully attached. The cells were treated with 10 μM PARE NPs for 4 h, then exposed to laser for 3 min. After laser treatments, the cells were stained with DiOC6 (3) and propidium iodide (PI) for 20 min to identify the live and dead cells by CLSM.

2.13. Calreticulin (CRT) dislocation induced by phototherapy of PARE NPs

SCC-7 cells (5×10^4 cells per well) were seeded in a 4-well microscopy chamber for 24 h until fully attached. Next, the SCC-7 cells were treated with 10 μM of PARE NPs for 4 h. Then, PARE NP-treated cells were irradiated with laser for 3 min. Thereafter, the cells were fixed and permeated with 3.7% paraformaldehyde for 20 min and 0.2% Triton-X 100 for 10 min, respectively. The CRT was stained with an Calreticulin (D3E6) XP Rabbit mAb (Alexa Fluor 488 Conjugate) (Cell Signaling Technology) for 12 h at 4 °C. The nuclei were stained with Hoechst 33342. The cell membrane was stained with DiD. The localization of CRT was observed by CLSM.

2.14. DC maturation promoted by the phototherapies of PARE NPs

For the evaluation of DC maturation, 10^6 of DC 2.4 cells were cultured with 10 μM R848 and PARE NPs for 24 h, respectively. LPS (50 ng/mL) treated DC 2.4 cells were set as the positive control. The marker of matured DC was analyzed by a flow cytometer. The matured DC were stained with Percp/Cy5.5-conjugated anti-CD80 antibody (Clone: 2D10) and analyzed by flow cytometry.

For the PDT-induced DC maturation, 2×10^4 of SCC-7 cells were seeded in the upper chamber of the Transwell plate overnight until fully attached. Then, the cells were treated with 10 μM PARE NPs for 24 h, followed by 4 min laser exposure. After that, the cell residues in the upper chamber were co-cultured with DC 2.4 cells (10^6 cells/well in the lower layer). LPS (50 ng/mL) treated DC 2.4 cells were set as the positive control. The matured DC were stained with Percp/Cy5.5-conjugated anti-CD80 antibody (Clone: 2D10) and analyzed with a flow cytometer.

2.15. Macrophage polarization effects of PARE NPs

Bone marrow-derived macrophages (BMDMs) were seeded in 12-well plates in DMEM with GM-CSF (20 ng/mL, BioLegend) for M0-like cells. The cells were changed with medium every other day. M1-type polarization was stimulated with LPS (100 ng/mL, Sigma-Aldrich) and IFN-γ (50 ng/mL, BioLegend) for 24 h, M2 -like polarization was stimulated with IL-4 (20 ng/mL, BioLegend). For the evaluation of M2 to M1 polarization,

the M2-type macrophage was treated with R848, PARE NPs for 24 h. The gene expression of specific markers for M1-like or M2-like was analyzed with RT-qPCR. Data are presented as the gene expression (fold change relative to GAPDH, as indicated). For morphological analysis of macrophages after treatment 48 h, cells were fixed with formaldehyde (15 min, 37 °C) and stained for actin with DyLight 554 Phalloidin (5.0 μg/mL, Cell Signaling Technology), and nuclei were stained with Hoechst 33342 (2 μg/mL, Thermo Scientific) for 15 min at room temperature. Plates were washed with PBS for CLSM observation.

2.16. The anti-tumor mechanism of PARE NPs in a co-culture system

For the co-cultured model of tumor cells and macrophages, 5×10^4 SCC-7/GFP cells and 1×10^4 macrophages (RAW264. 7) were seeded in the 6-well plate overnight, then treated with PARE NPs for 24 h. The drug was washed with PBS twice and replaced with fresh medium, the laser-treated groups were exposed to 680 nm laser for 3 min. After 12 h, the cells were collected for flow cytometry. The live cancer cells were counted by monitoring the fluorescence signaling of GFP from SCC-7/GFP cells. To exclude the sole phototherapeutic effect of PARE NPs, the SCC-7/GFP cells (without macrophages) were set and treated with PARE NPs+L.

2.17. HNSCC tumor model establishment

Female H3C mice (6-8 weeks) were purchased from Harlan (Livermore, CA, USA). All animal experiments strictly followed the guidelines of Animal Use and Care Administrative Advisory Committee (AAALAC) of University of California, Davis and Shanghai Jiao Tong University. All animals were kept under pathogen-free conditions and were allowed to acclimatize for at least 5 days prior to any experiments. The SCC-7 tumor mouse models were established by subcutaneous inoculating 4×10^5 SCC-7 cells in 50 μL of PBS with 10% Matrigel into both left and right flanks of each mouse.

2.18. Pharmacokinetics (PK) profile of PARE NPs

PARE NPs (10 mg/kg) were i.v injected into healthy balb/c mice, free PA was employed as a surrogate of free drug control. Certain amounts of blood samples were collected at different times and dissolved with DMSO. The concentrations of PA-R848 prodrugs were calculated according to a fluorescence-based standard curve. The fluorescence of PA was determined by a fluorescence spectrophotometer. The PK parameters were analyzed by the Kinetica TM software package (version5.0 Thermo Fisher Scientific Inc., MA, USA).

2.19. Biodistribution of PARE NPs

NIRF imaging was employed to investigate the biodistribution of PARE NPs on SCC-7 tumor-bearing mice. The fluorescence signal of PA at the tumor site was monitored at different time points. Animals were euthanized after 48 h of the material injection, major organs and tumors were collected for ex-vivo imaging. The biodistribution of PARE NPs was evaluated by quantifying the fluorescence signal of PA. For tumor tissue cryo-section, harvested tumors were embedded in OCT agent and frozen at w− 80 °C. The thickness of tissue slices is 10 μm. The nuclei were stained with Hoechst 33342 (2 μg/mL, Thermo Scientific).

2.20. In vivo anti-tumor efficacy of PARE NPs

The SCC-7 tumor-bearing mice were randomly distributed into 8 groups (n=8) for the evaluation of anti-tumor efficacy of PARE NPs. When the tumors volume reached ~50 mm^3, PARE NPs (10 mg/kg) and the control materials were i.v. administrated once per week, mice were irradiated with a 680 nm laser (0.5 W/cm^2) for 3 min after 24 and 48 h of the drug administration, determined by in vivo imaging results. Anti-PD-1 antibody was administrated by i.p. injection at a dose of 200 μg/mouse twice a week. 8 groups were noted as follows: PBS, anti-PD-1 antibody (Anti-PD-1), free PA+R848 with or without laser treatment (Mix/(Mix+L), PARE NPs with or without laser treatment (PARE NPs/PARE NPs+L), the combination of PARE NPs and anti-PD-1 antibody with or without laser treatment (PARE NPs+anti-PD-1/PARE NPs +anti-PD-1+L). The body weight and tumor sizes were accurately monitored twice per week. The calculation formula of tumor volume was: $width^2 \times length/2$.

2.21. Flow cytometry analysis

To evaluate the immune response, distant tumors and tumor-draining lymph nodes (TDLNs) were collected and digested using 1500 U/mL collagenase, 1000 U/mL hyaluronidase, and DNase at 37 °C for 40 min. The single cell was obtained by filtering through nylon mesh filters and washing with PBS (1% FBS). For T cell anlysis, the single-cell suspension was incubated with anti-CD45-FITC (Biolegend), anti-CD3-FITC (Biolegend), anti-CD8a-APC (Biolegend), anti-CD4-PerCP (Biolegend), anti-CD25-comp-APC (Biolegend) and anti-Foxp3-PE (Biolegend) antibodies. For DC anlysis, the single-cell suspension was incubated with anti-CD45-AF700 (Biolegend), anti-CD11c-AF488 (Biolegend), anti-MHCII-APC-Cy7 (Biolegend), Anti-CD80-PerCPCy5.5 (Biolegend). Then, those cells were washed with PBS containing 1% FBS and analyzed using fluorescence-activated cell sorting (FACS) analysis. Data analysis was performed by FlowJo software (Version 10.0).

2.22. Cytokines analysis by RT-qPCR

The specific cytokines of DC and M1/M2 TAMs were analyzed with RT-qPCR. Data are presented as the gene expression (fold change relative to GAPDH, as indicated). Gene sequence: GAPDH (Forward: AGGTCGGTGTCAACGGATTT Reverse: CCTTCCACGATGCCAAAGTT). CD206 (Forward: AAAACTGACTGGGCTTCCGT Reverse: CCTCTCGAGCACAGGTCATC). NOS2 (Forward: AGGTTGTCTGCATGGACCAG Reverse: GCTGGGACAGTCTCCATTCC). IL-12 (Forward: CAACCATCAGCAGATCATTCTA Reverse: GAGTCCAGTCCACCTCTACAAC). CD80 (Forward: AATCAGCACCTGACCTGGAC Reverse: CTGTCTGCGTATTGCAGCAT).

2.23. Immunohistochemistry assay

The tumor tissues were fixed in 4% (W/V) paraformaldehyde over 48 h, then embedded in paraffin. The prepared sections from paraffin-embedded tumors were stained with Ki67. In detail, the sections were de-waxed and rehydrated with xylene successively, then a graded series of ethanol and deionized water. The endogenous peroxidase was quenched with 3% hydrogen peroxide (H_2O_2) for 10 min and washed with deionized water. The slides

were microwaved for 5 min and blocked for 1 h with blocking buffer (5% normal goat serum). Next, the slides were incubated with rabbit polyclonal antibody against (1:100, 1:200, 1:200) at 4 °C overnight. After washing with PBS, biotinylated goat anti-rabbit IgG (1:1000, Abcam) was incubated with the sections for 30 min at room temperature. Then, the sections were stained with diaminobenzidine (DAB) and counterstained with hematoxylin. The positivity was indicated by the presence of brown staining.

2.24. In vivo biocompatibility evaluation

The biosafety of PARE NPs was evaluated by treating healthy FBV mice with free PA, PARE NPs (10 mg/kg) and PBS, respectively, and their body weight, hematological & biochemical parameters and histopathology were measured as references.

2.25. Statistical analysis

All results were presented with the mean ± standard deviation. Prism GraphPad (GraphPad software, CA, USA) and Excel 2016 (Microsoft Corporation, WA, USA) were used for all statistical analyses. Statistical analysis was performed by Student's t-test for two groups, and one-way ANOVA for multiple groups. The value of $P < 0.05$(*) was considered statistically significant, the value of $P < 0.01$(**) and $P < 0.001$(***) was considered statistically more significant.

3. Results and discussion

3.1. Fabrication and characterization of PARE NPs

The synthetic route of PA-R848 prodrug was shown in Fig. S1. To avoid conjugating R848 with PA by forming an amide bond that is difficult to hydrolyze, the amine groups on R848 were protected and the hydroxyl group was attached to the carboxylic acid on the PA molecules. The characterization data, including mass spectra (Figs. S2, S3), nuclear magnetic resonance (NMR) spectrum (Fig. S4) and thin-layer chromatography (TLC) traces (Fig. S5), supported that the esterase-responsive PA-R848 prodrug was successfully synthesized. Since the PA-R848 prodrugs were completely new molecules, their hemolysis profiles on RBCs were conducted to evaluate biocompatibility. As shown in Fig. S6, the PA-R848 prodrugs induced imperceptible hemolysis at different concentrations, suggesting that the PA-R848 prodrugs showed good biocompatibility, which was safe for i.v. administration. In addition, the cytotoxicity of PA-R848 prodrugs on SCC-7 cells was investigated. As shown in Fig. S7, the PA-R848 prodrugs showed very less toxicity to the cells. In contrast, they exhibited strong toxicity upon the laser irradiation, indicating that the PA-R848 prodrugs were non-toxic if we didn't trigger the phototherapeutic effect. The PA-R848 prodrug can readily assemble into small molecule nanomedicine (PARE NPs) driven by the π-π stacking and hydrophobic interactions [22]. The PARE NPs harbored 100% active pharmaceutical ingredients, in which the phototherapeutic agent and immune-agonist were 62.4% and 38.6%, respectively. The particle size and PDI of PARE NPs were measured as ~120 nm and 0.197, respectively (Fig. 1a), indicating that the nanoparticles were well constructed and monodispersed. The surface charge of PARE NPs was around 18.66 mV. The morphology of PARE NPs was spherical, observed by TEM (Fig. 1b). The UV–vis spectra (Fig. 1c) showed that the Q-band of PA in PARE NPs obviously shifted to red,

providing evidence for the self-assembly of PA in PARE NPs. The fluorescence spectra (Fig. 1d) revealed that the emission of PA was around 680 nm, the fluorescence signal of PARE NPs decreased more than 15-fold, indicating the "π-π" stacking of PA in PARE NPs. While the fluorescence signal of Pa recovered after incubation with 10% SDS. The redshift in UV–vis spectra and fluorescence quenching phenomenon supported the successful assembly of PARE NPs. The critical aggregation concentrations (CAC) of PARE NPs were determined to be ~2.4 μM (Fig. 1e). The stability of PARE NPs with or without 10% FBS was monitored by DLS for 14 consecutive days. The particle size of PARE NPs with 10% FBS increased slightly due to the adhesion of serum proteins, but the size didn't fluctuate notably over 14 days (Fig. 1f). In parallel, the surface charge of PARE NPs did not change significantly as well (Fig. S8), further supporting that our nanoparticles were with good stability.

3.2. Phototherapeutic effect of PARE NPs

As a photosensitizer, PA was supposed to exhibit strong photodynamic and photothermal therapeutic effects upon laser irradiation. Hence, the photothermal effect of PARE NPs was investigated by monitoring the hyperthermia generation with a thermal imaging camera. Fig. 1g showed that the photo-induced hyperthermia of PARE NPs increased in a concentration-dependent manner. The temperature of PARE NPs (50 μM) solution increased by more than 22 °C, indicating the PARE NPs could effectively transform the photonics to hyperthermia. Photodynamic effect of PARE NPs was performed by detecting the reactive oxygen species (ROS) production indicated by SOSG probe. As shown in Fig. 1h, laser-exposed PARE NPs produced copious amounts of ROS in a concentration-dependent manner. These results suggested that PARE NPs would exhibit potent phototherapeutic effects that effectively eradicate tumor tissue.

3.3. Esterase-responsive drug release of PARE NPs

Since the PA-R848 prodrug was synthesized by coupling PA and R848 via an ester bond, the drug release of PARE NPs was studied under physiological conditions and esterase-rich environments. As depicted in Fig. 1i, the PARE NPs remained stable and exhibited negligible R848 release in PBS (pH 7.4), indicating that PA and R848 would be encapsulated within the nanostructure and remain inactive under physiological conditions. R848 was sustainably released with time elapse after the addition of esterase, then reached a plateau at 72 h and showed more than 80% drug release. Since the intratumoral esterase concentration is considerably higher than that of normal cells [43], the esterase-responsiveness of PARE NPs would prevent premature drug release or leakage before reaching tumor site.

3.4. Cell uptake, phototherapeutic effects and cytotoxicity on SCC-7 cancer cells

The cell uptake of PARE NPs was investigated on SCC-7 cells. Fig. 2a showed that the PARE NPs could be ingested by SCC-7 cells and mainly distributed in cytoplasm and lysosomes in a time-dependent manner (Fig. 2b). The phototherapeutic effects of PARE NPs were then evaluated. Fig. 2c demonstrated that laser-irradiated PARE NPs could induce a concentration-dependent abundance of ROS at the cellular level. Then, we irradiated a discrete area of SCC-7 cells that had been pre-incubated with free Pa and PARE NPs; DIC6(3) and PI were used to identify living and dead cells, respectively. As indicated in Fig.

2d, the majority of SCC-7 cells treated with PARE NPs and laser were dead compared to the control group, whereas the PARE NPs (without laser) treated cells exhibited significantly less cell mortality. The results indicated that the phototherapy of PARE NPs was highly controllable, affecting only the laser-directing area. The cytotoxicity of PARE NPs was investigated further and is depicted in Fig. 2e. Laser treatment enhanced the anticancer efficacy of PARE NPs in a concentration-dependent manner. In contrast, PARE NPs without laser exhibited minimal cytotoxicity at concentrations as high as 50 μM. The cell assays suggested that PARE NPs could be efficiently ingested by SCC-7 cells, promote ROS production, and result in cell death due to their exceptional phototherapeutic effects.

3.5. TAM polarizing effect of PARE NPs on BMDMs

The TAM polarizing effect of PARE NPs was investigated on murine bone marrow-derived macrophages (BMDMs). BMDMs from Balb/c mice were treated with GM-CSF, LPS + IFN-r, and IL-4 to generate M0-macrophages, anti-tumorigenic M1-like, and protumorigenic M2-like macrophages, respectively (Fig. S9). It has been reported that the M1- and M2-like macrophages showed distinguishable morphology differences [12]. Therefore, the cell morphology was observed to evaluate the polarization status of M2- into M1-like cells by CLSM (Fig. 2f). First, the M1- and M2- like macrophages were observed respectively; the M1-like cells showed round shape, while the M2-like cells are more stretched in morphology. Then, M2-like cells were incubated with PARE NPs, the R848 treated cells were set as a positive control. As shown in Fig. 2f, more M1-like cells with round-shape were observed in both free PARE NPs and R848 treated cells, indicating that PARE NPs could effectively polarize M2 into M1-like cells as similar to R848. To further confirm the phenotypes polarization effect of PARE NPs, the specific marker expression of M2 or M1-like cells was analyzed by RT-qPCR. Fig. 2g showed that the specific marker (CD206) expression of M2-like cells was downregulated, while the specific marker (NOS2, Fig. 2h) and proinflammatory cytokines (IL-12, Fig. 2i) expression of M1-like cells were upregulated after incubation with PARE NPs. These findings provided additional evidence that PARE NPs can release R848 to stimulate the polarization of M2 cells into M1-like cells. By regulating the phenotypic polarization of TAM, it is possible to inhibit TAM-mediated tumor angiogenesis efficiently. In contrast, the enrichment of M1-like cells not only induced the expression of proinflammatory cytokines, which is beneficial to the recruitment and proliferation of CTL. It was hypothesized that PARE NPs may be helpful for boosting immune responses.

3.6. Immunogenic cell death (ICD) triggered by phototherapy

Phototherapy can induce immunogenic cell death (ICD) in tumor cells, thereby stimulating a robust immune response. Calreticulin (CRT) is usually expressed on the endoplasmic reticulum, and distributed in the cytoplasm. CRT will transport to the cell surface in response to ER stress, which is considered an indicator of ICD, as tumor cells undergo ICD [36, 44]. Immunofluorescence was used to detect the location of CRT on SCC-7 cells in order to investigate the ICD effect induced by phototherapy using PARE NPs. As shown in Fig. 3a, CRT in the PBS+L and PARE NPs-treated groups were evenly distributed in the cytoplasm, while in the PARE NPs+L treated group, the distribution of CRT was observed in

the vicinity of the cell membrane, suggesting that the phototherapy based on PARE NPs can effectively elicit ICD effect.

3.7. DC maturation effects of PARE NPs

We investigated whether phototherapy-induced ICD and R848 can promote DC maturation. First, the efforts of ICD were investigated in a Transwell system (Fig. 3b), SCC-7 cells were seeded in the upper chamber and treated with PARE NPs&laser irradiation, the DC2.4 cells were seeded in the lower chamber to ingest the TAAs that phototherapy generated. The marker (CD80+) of matured DC was analyzed by FACS (Figs. 3c and 3d). Due to the efforts of the released R848, the PARE NPs demonstrated significantly higher potent in mDC promotion than the PBS-treated cells. In striking contrast, the PARE NPs+L treatment substantially upregulated the expression of the CD80+ marker, suggesting that the phototherapy-triggered ICD predominately contributed to the development of the mDC. The TLR7/8 activation can effectively promote DC maturation as well, which is beneficial to the recruitment and migration of DC to lymph nodes for further antigen presentation. [13, 30] The mDC-promoting effect of R848 was further evaluated by directly incubating R848 or PARE NPs with DCs (Fig. 3e and Fig. S10). The CD80+ on free R848-treated cells significantly increased in comparison to PBS-treated cells, while the PARE NPs exhibited similar efforts with R848 on the mDC promotion, suggesting that free and released R848 can both promote DCs from immature to mature state. These results demonstrated that phototherapy-induced ICD and R848 could substantially promote DC maturation and elicit immune responses.

3.8. The working mechanism of PARE NPs evaluated in a co-culture system

We set up a co-culture system to validate the working mechanism of PARE NPs. The SCC-7/GFP tumor cells and macrophages were co-cultured and applied to different treatments, the GFP fluorescence of live tumor cells was collected by flow cytometry to reveal the cell-killing effects. As shown in Figs. 3f and 3g, the PARE NPs treated groups showed obviously more cell-killing compared to the PBS group, indicating that the PARE NPs could strengthen the macrophages to kill tumor cells. To exclude the anti-tumor effect of phototherapy, the SCC-7/GFP cells (without macrophages) were treated with PARE NPs+L, showing that the phototherapy can substantially kill the tumor cells. The co-culture system treated with PARE NPs+L demonstrated that the combining effects of phototherapy and R848-activated macrophages exhibited the most substantial efforts on tumor cell killing. The co-culture experiments revealed that the PARE NPs could inhibit tumor cell proliferation *via* two pathways: i) phototherapy of PA and ii) macrophage-mediated effects of R848. Collectively, the phototherapeutic effects of PARE NPs could directly kill the tumor cells and activate ICD to further release the TAA for mDC stimulation. R848 from PARE NPs could polarize macrophages from M2 into M1 subtype and facilitate the maturation of DC. These mechanisms could effectively strengthen immune response by synergistic effect between ICD and polarization (Fig. 3h).

3.9. In vivo pharmacokinetic (PK) profile of PARE NPs

To evaluate whether our small molecule nanomedicine can improve the PK profile of the free drugs, PARE NPs (10 mg/kg) were iv. injected to balb/c mice. The equivalent

concentration of free PA was i.v. administered as a control. As shown in PK results (Fig. 4a), free PA was rapidly cleared during blood circulation, while the PARE NPs exhibited a significantly longer circulation time. The PK parameters (Fig. 4b) showed that the area under the curve ($AUC_{0-\infty}$) of free PA and PARE NPs was calculated to be 93.26±6.51 and 262.8±53.38 g/mL·h, respectively. The PARE NPs showed 2.82 times larger AUC than the free drug counterpart (PA). The PARE NPs ($T_{1/2}$ is 0.34±0.19 h) showed 2.1-time longer half-time than the free PA ($T_{1/2}$ is 0.16±0.01 h). The PK results demonstrated that PARE NPs could improve the blood circulation profile of free drugs, which is beneficial to the tumor accumulation of the therapeutics. The PARE NPs can effectively improve the druggability of the hydrophobic drugs, but the positively charged surface made them relatively detrimental to the opsonization effect[45, 46]. Therefore, the PARE NPs improved the PK profile of the free drug to some extent, but not as good as the liposomal formulations[47].

3.10. Biodistribution evaluation of PARE NPs by NIRF

Furthermore, the tumor accumulation of PARE NPs was evaluated by NIRF imaging on mice bearing SCC-7 tumors. Compared to free PA, the NIRF imaging of PARE NPs demonstrated that the fluorescence signal increased in a time-dependent manner (Fig. 4c). At 48 h post-injection, the tumor fluorescence of the PARE NPs treated mice was 7-fold more remarkable than that in the free PA group (Fig. 4d). *Ex vivo* NIRF imaging was utilized to evaluate the biodistribution of PARE NPs in major organs and tumors 48 h after administration. In contrast to free PA, the PARE NPs group exhibited a more distinct fluorescence signal in the liver and kidney, particularly in tumors (Fig. 4e). The quantitative fluorescence intensity of tumors in the PARE NPs group was 4.33-fold higher than in the free PA group (Fig. 4f), indicating the specific accumulation of PARE NPs in tumor tissues. The liver accumulation of PARE NPs was ascribed to the reticuloendothelial system (RES) capture. The fluorescence signal of PARE NPs in the kidney suggested that PARE NPs may be eliminated via the kidney. The tumor tissue infiltration of PARE NPs was evaluated in Fig. 4g, the fluorescence in the cryosection of tumor tissue revealed that PARE NPs exhibited significantly greater tumor accumulation than free PA. The animal imaging results supported that PARE NPs can effectively accumulate at tumor sites and infiltrate profoundly into tumor tissue due to the altered vasculature and impaired lymphatic drainage.

3.11. The anti-tumor effect of the phototherapy-promoted immunotherapy

The SCC-7 tumor models were established to investigate the synergistic phototherapy-promoted immunotherapy based on the encouraging PK profile and tumor accumulations of PARE NPs. Fig. 5a depicted the animal experimentation procedure. Each mouse was inoculated with SCC-7 cells on the left (primary) and right (distant) flanks. When the tumor volume reached 50 mm^3, mixed free drugs (PA+R848) or PARE NPs formulation were i.v. injected once per week, followed by exposure to a 680 nm laser (0.5 W/cm^2) for 3 min at 24 h and 48 h post-injection; The timing of laser irradiation was determined by the in vivo imaging results in Fig. 4c. To enhance the immunotherapy, anti-PD-1 (CD279) was injected intraperitoneally (i.p.) into mice at a dose of 100 μg/mouse twice per week. PBS, Anti-PD-1, Mix/Mix+L, PARE NPs/PARE NPs+L, PARE NPs+anti-PD-1/PARE NPs+anti-PD-1+L were the 8 groups identified. The growth of primary and distant

tumors in various groups was measured twice per week. The temperature of tumors was measured using an infrared thermal camera (Fotric 225). When compared to the Mix (Free PA mixed with R848) group, the temperature of tumors treated by PARE NPs and PARE NPs+anti-PD-1 increased by 38 °C rapidly (Fig. 5b), which may be attributed to the high accumulation of PARE NPs at the tumor site. The increased temperature was sufficient enough to ablate tumors. As depicted in Fig. 5c, PARE NPs+L and PARE NPs+anti-PD-1+L groups ablated primary tumors completely. In parallel, the laser-ablated primary tumors were accompanied by delayed development of non-laser-treated distant tumors (Fig. 5d), particularly in the PARE NPs+anti-PD-1+L group, where distant tumor progress was notably retarded. In striking contrast, the growth of distant tumors in other groups was rapid, whereas the growth rate was slowed in the Mix+L and PARE NPs+L treated mice. There was no apparent deviation in the body weight in all groups (Fig. 5e), demonstrating that our treatments were highly biocompatible. At the endpoint, histological examinations of tumors were investigated. Compared to other groups, the tumor cells in the PARE NPs+anti-PD-1+L group were markedly destroyed (Fig. 5f). The encouraging data showed that the phototherapy of PARE NPs directly ablated the primary tumor and the phototherapy-promoted immunotherapy effectively retarded the progress of the distant tumor, suggesting that the synergistic approach of PARE NPs would be a potent approach for HNSCC treatment.

3.12. Synergistic mechanisms of phototherapy-promoted immnunotherapy

To comprehend the synergistic mechanism of phototherapy-promoted immunotherapy based on PARE NPs, the distant tumor tissues of PBS, PARE NPs+L and PARE NPs+L+anti-PD-1 treated mice were harvested on Day 15 and analyzed by FACS. The gating process was shown in Fig. S11. PARE NPs+L and PARE NPs+anti-PD-1+L treated tumors showed a remarkable increase in the percentage of CD3+T cells. Especially in the PARE NPs+anti-PD-1+L treat mice (Fig. 6a and Fig. S12), the CD3+ T cell population increased from 16.01% to 61.37% compared to the PBS treatment, indicating that more T cells infiltrated into tumor tissues. CD4+ T cells played a crucial role in the regulation of immune responses. A significantly larger population of CD4+ T cells was found in the PARE NPs+L (61.42%) and PARE NPs+anti-PD-1+L (57.11%) treated tumors, compared to the PBS (38.22%) control (Fig. 6b and Fig. S13). CD8+ T cells can specifically recognize and destroy tumor cells. As shown in Fig. 6c and Fig. S13, the PARE NPs+anti-PD-1+L recruited more CD8+ T cells (38.64%) infiltrating into tumor tissues than either PARE NPs+L (30.76%) or and PBS (22.04%). The percentage of regulatory T cells (Tregs, CD3+CD4+Foxp3+) that inhibit immune responses decreased in the PARE NPs+L and PARE NPs+anti-PD-1 treated tumors (Fig. 6d Fig. S14). Specifically, for the PARE NPs+anti-PD-1+L group, the population of Tregs decreased dramatically to 2.39%, indicating that the PARE NPs and anti-PD-1 significantly suppressed the immune-suppressive activity of TIME. Moreover, the ratios of CD4+ CTL/Treg and CD8+CTL/Treg were significantly increased in tumors of mice treated with PARE NPs+anti-PD-1+L (Figs. 6e and 6f). The changes in T cells demonstrated that the PARE NPs+L could effectively enhance the anti-tumor immune response and suppress the pro-tumor immune activity, and such effect can be reinforced if combined with ICB.

To further corroborate the synergistic mechanisms, the immune-related gene expression in the tumors was analyzed by RT-qPCR. The expression of CD4 and CD8 of PARE NPs+L and PARE NPs+L+anti-PD-1+L treated groups increased significantly (Figs. 6g and 6h), while Foxp3 expression decreased (Fig. 6i). These results were consistent with the FACS results, indicating that PARE NPs could effectively prime the T cells. The expression of CD80 (Fig. 6j), IL-12 (Fig. 6k), and NOS2 (Fig. 6l) in PARE NPs+L and PARE NPs+anti-PD-1+L treated groups increased significantly, suggesting that more matured DC and M2 TAMs could be activated by PARE NPs, especially when combined with ICB. The immunohistochemistry (IHC) assay revealed less Ki67 expressed in tumor tissues when treated with PARE NPs+L+anti-PD-1, indicating that our strategy resulted in improved anti-tumor effectiveness (Fig. 6m). Furthermore, we collected tumor-draining lymph nodes and analyzed the DC maturation using FACS. As shown in Fig. S15, the mDC population in lymph nodes significantly increased in PARE NPs +L and PARE NPs +anti-PD-1+L treated groups, indicating that phototherapy combined with TLR7/8 activation in PARE NPs could effectively activate the systemic immunity and promoted DC maturation. The above findings demonstrated that the synergistic phototherapy-promoted immunotherapy based on PARE NPs could stimulate immunological responses and elicit outstanding anti-tumor effects on both primary and distant metastatic tumors.

3.13. The biocompatibility of PARE NPs

The potential toxicity of PARE NPs (10 mg/kg) was evaluated on healthy mice by comparison of body weight, hematology and biochemical analysis, and histopathology of main organs (heart, lung, liver, spleen and kidney). The mice gained weight in all three groups (Fig. 7a). The hematological results showed that the major blood cells number of PARE NPs-treated group did not differ significantly from those of the PBS and Mix groups (Figs. 7b-g), indicating that our nanoformulation did not induce acute toxicity. Moreover, the biochemical parameters for liver and kidney in PARE NPs-treated mice did not exhibit abnormal fluctuation compared with PBS and Mix groups (Figs. 7h-k), suggesting that PARE NPs did not cause acute function impairment of liver and kidney after i.v. injection, even though PARE NPs showed accumulations in the liver and kidneys. Furthermore, the histopathology of main organs was evaluated, the PARE NPs induced no discernible tissue damage in healthy mice, even in the accumulated organs as demonstrated in the H&E results (Fig. 7l). Collectively, PARE NPs have been identified as a promising photo-/immune-therapeutic agents with high biocompatibility.

4. Conclusions

In this work, we constructed a drug-drug conjugates self-assembled nanomedicine (PARE NP) with 100% drug loading to accomplish synergistic phototherapy-promoted immunotherapy. PARE NPs effectively suppressed the growth of HNSCC tumors at in vitro and in vivo levels. PARE NPs could polarize TAM subtypes from M2 to M1 with the efforts of R848, directly ablate tumors by powerful phototherapeutic effects and promote DC from immature to mature by the combined efforts of R848 and phototherapy-induced ICD. In addition, the PARE NPs effectively improved the pharmacokinetic performance and increased the tumor accumulation of the therapeutics. In vivo antitumor effect revealed that

the biocompatible PARE NPs exhibited synergistic phototherapy-promoted immunotherapy, which completely eradicated primary tumors and effectively suppressed distant tumors. Our formulations showed great promise in the treatment of head and neck malignancies.

Supplementary Material

Refer to Web version on PubMed Central for supplementary material.

Acknowledgements

The authors gratefully acknowledge the support from the National Natural Science Foundation of China (82172084, 81803002), STI2030-Major Projects (2022ZD0212500) and the startup funding of Shanghai Jiao Tong University.

References

[1]. DeFrancesco L, CAR-T cell therapy seeks strategies to harness cytokine storm, Nat Biotechnol, 32 (2014) 604–604. [PubMed: 25004212]

[2]. Melero I, Berman DM, Aznar MA, Korman AJ, Gracia JLP, Haanen J, Evolving synergistic combinations of targeted immunotherapies to combat cancer, Nat Rev Cancer, 15 (2015) 457–472. [PubMed: 26205340]

[3]. Ye YQ, Wang JQ, Hu QY, Hochu GM, Xin HL, Wang C, Gu Z, Synergistic Transcutaneous Immunotherapy Enhances Antitumor Immune Responses through Delivery of Checkpoint Inhibitors, ACS Nano, 10 (2016) 8956–8963. [PubMed: 27599066]

[4]. Kim J, Hong J, Lee J, Fakhraei Lahiji S, Kim Y-H, Recent advances in tumor microenvironment-targeted nanomedicine delivery approaches to overcome limitations of immune checkpoint blockade-based immunotherapy, J. Control. Release, 332 (2021) 109–126. [PubMed: 33571549]

[5]. Zou W, Immunosuppressive networks in the tumour environment and their therapeutic relevance, Nat. Rev. Cancer, 5 (2005) 263–274. [PubMed: 15776005]

[6]. De Palma M, Lewis CE, Macrophage Regulation of Tumor Responses to Anticancer Therapies, Cancer Cell, 23 (2013) 277–286. [PubMed: 23518347]

[7]. Zheng Y, Han Y, Sun Q, Li Z, Harnessing anti-tumor and tumor-tropism functions of macrophages via nanotechnology for tumor immunotherapy, Exploration, 2 (2022) 20210166. [PubMed: 37323705]

[8]. Frank AC, Ebersberger S, Fink AF, Lampe S, Weigert A, Schmid T, Ebersberger I, Syed SN, Brune B, Apoptotic tumor cell-derived microRNA-375 uses CD36 to alter the tumor-associated macrophage phenotype, Nat. Commun, 10 (2019) 1135. [PubMed: 30850595]

[9]. Murray PJ, Allen JE, Biswas SK, Fisher EA, Gilroy DW, Goerdt S, Gordon S, Hamilton JA, Ivashkiv LB, Lawrence T, Locati M, Mantovani A, Martinez FO, Mege JL, Mosser DM, Natoli G, Saeij JP, Schultze JL, Shirey KA, Sica A, Suttles J, Udalova I, van Ginderachter JA, Vogel SN, Wynn TA, Macrophage Activation and Polarization: Nomenclature and Experimental Guidelines, Immunity, 41 (2014) 14–20. [PubMed: 25035950]

[10]. Wynn TA, Chawla A, Pollard JW, Macrophage biology in development, homeostasis and disease, Nature, 496 (2013) 445–455. [PubMed: 23619691]

[11]. Zhang MY, He YF, Sun XJ, Li Q, Wang WJ, Zhao AM, Di W, A high M1/M2 ratio of tumor-associated macrophages is associated with extended survival in ovarian cancer patients, J. Ovarian Res, 7 (2014) 1–16. [PubMed: 24401654]

[12]. Rodell CB, Arlauckas SP, Cuccarese MF, Garris CS, Ahmed RLMS, Kohler RH, Pittet MJ, Weissleder R, TLR7/8-agonist-loaded nanoparticles promote the polarization of tumour-associated macrophages to enhance cancer immunotherapy, Nat. Biomed. Eng, 2 (2018) 578–588. [PubMed: 31015631]

[13]. Sato-Kaneko F, Yao SY, Ahmadi A, Zhang SS, Hosoya T, Kaneda MM, Varner JA, Pu M, Messer KS, Guiducci C, Coffman RL, Kitaura K, Matsutani T, Suzuki R, Carson DA, Hayashi T, Cohen

EEW, Combination immunotherapy with TLR agonists and checkpoint inhibitors suppresses head and neck cancer, JCI Insight, 2 (2017) e93397. [PubMed: 28931759]

[14]. Prins RM, Craft N, Bruhn KW, Khan-Farooqi H, Koya RC, Stripecke R, Miller JF, Liau LM, The TLR-7 agonist, imiquimod, enhances dendritic cell survival and promotes tumor antigen-specific T cell priming: Relation to central nervous system antitumor immunity, J. Immunol, 176 (2006) 157–164. [PubMed: 16365406]

[15]. Trinchieri G, Sher A, Cooperation of Toll-like receptor signals in innate immune defence, Nat. Rev. Immunol, 7 (2007) 179–190. [PubMed: 17318230]

[16]. Bellmunt J, de Wit R, Vaughn DJ, Fradet Y, Lee JL, Fong L, Vogelzang NJ, Climent MA, Petrylak DP, Choueiri TK, Necchi A, Gerritsen W, Gurney H, Quinn DI, Culine S, Sternberg CN, Mai Y, Poehlein CH, Perini RF, Bajorin DF, K.-. Investigators, Pembrolizumab as Second-Line Therapy for Advanced Urothelial Carcinoma, New Engl. J. Med, 376 (2017) 1015–1026. [PubMed: 28212060]

[17]. Rittmeyer A, Barlesi F, Waterkamp D, Park K, Ciardiello F, von Pawel J, Gadgeel SM, Hida T, Kowalski DM, Dols MC, Cortinovis DL, Leach J, Polikoff J, Barrios C, Kabbinavar F, Frontera OA, De Marinis F, Turna H, Lee JS, Ballinger M, Kowanetz M, He P, Chen DS, Sandler A, Gandara DR, Grp OS, Atezolizumab versus docetaxel in patients with previously treated non-small-cell lung cancer (OAK): a phase 3, open-label, multicentre randomised controlled trial, Lancet, 389 (2017) 255–265. [PubMed: 27979383]

[18]. Dai H, Fan Q, Wang C, Recent applications of immunomodulatory biomaterials for disease immunotherapy, Exploration, 2 (2022) 20210157. [PubMed: 37324799]

[19]. Ledford H, Therapeutic cancer vaccine survives biotech bust, Nature, 519 (2015) 17–18. [PubMed: 25739610]

[20]. Castano AP, Mroz P, Hamblin MR, Photodynamic therapy and anti-tumour immunity, Nat. Rev. Cancer, 6 (2006) 535–545. [PubMed: 16794636]

[21]. Jing L, Qu H, Wu D, Zhu C, Yang Y, Jin X, Zheng J, Shi X, Yan X, Wang Y, Platelet-camouflaged nanococktail: Simultaneous inhibition of drug-resistant tumor growth and metastasis via a cancer cells and tumor vasculature dual-targeting strategy, Theranostics, 8 (2018) 2683–2695. [PubMed: 29774068]

[22]. Qu H, Chen H, Cheng W, Wang Y, Xia Y, Zhang L, Ma B, Hu R, Xue X, A supramolecular assembly strategy for hydrophilic drug delivery towards synergistic cancer treatment, Acta Biomater., 164 (2023) 407–421. [PubMed: 37088157]

[23]. Jing LJ, Qu HJ, Wu DQ, Zhu CJ, Yang YB, Jin X, Zheng J, Shi XS, Yan XF, Wang Y, Platelet-camouflaged nanococktail: Simultaneous inhibition of drug-resistant tumor growth and metastasis via a cancer cells and tumor vasculature dual-targeting strategy, Theranostics, 8 (2018) 2683–2695. [PubMed: 29774068]

[24]. Chen Q, Xu LG, Liang C, Wang C, Peng R, Liu Z, Photothermal therapy with immune-adjuvant nanoparticles together with checkpoint blockade for effective cancer immunotherapy, Nat. Commun, 7 (2016) 13193. [PubMed: 27767031]

[25]. Chao Y, Xu LG, Liang C, Feng LZ, Xu J, Dong ZL, Tian LL, Yi X, Yang K, Liu Z, Combined local immunostimulatory radioisotope therapy and systemic immune checkpoint blockade imparts potent antitumour responses, Nat. Biomed. Eng, 2 (2018) 611–621. [PubMed: 31015634]

[26]. He C, Duan X, Guo N, Chan C, Poon C, Weichselbaum RR, Lin W, Core-shell nanoscale coordination polymers combine chemotherapy and photodynamic therapy to potentiate checkpoint blockade cancer immunotherapy, Nat. Commun, 7 (2016) 12499. [PubMed: 27530650]

[27]. Chao Y, Xu L, Liang C, Feng L, Xu J, Dong Z, Tian L, Yi X, Yang K, Liu Z, Combined local immunostimulatory radioisotope therapy and systemic immune checkpoint blockade imparts potent antitumour responses, Nat. Biomed. Eng, 2 (2018) 611–621. [PubMed: 31015634]

[28]. Wang H, Han X, Dong Z, Xu J, Wang J, Liu Z, Hyaluronidase with pH-responsive Dextran Modification as an Adjuvant Nanomedicine for Enhanced Photodynamic-Immunotherapy of Cancer, Adv. Funct. Mater, 29 (2019) 1902440.

[29]. Wu JJ, Huang DB, Tyring SK, Resiquimod: a new immune response modifier with potential as a vaccine adjuvant for Th1 immune responses, Antivir. Res, 64 (2004) 79–83. [PubMed: 15498602]

[30]. Phuengkham H, Song C, Lim YT, A Designer Scaffold with Immune Nanoconverters for Reverting Immunosuppression and Enhancing Immune Checkpoint Blockade Therapy, Adv. Mater, 31 (2019) 1903242.

[31]. Shi J, Kantoff PW, Wooster R, Farokhzad OC, Cancer nanomedicine: progress, challenges and opportunities, Nat. Rev. Cancer, 17 (2017) 20–37. [PubMed: 27834398]

[32]. Xue X, Qu H, Li Y, Stimuli-responsive crosslinked nanomedicine for cancer treatment, Exploration, 00 (2022) 20210134.

[33]. Nam J, Son S, Park KS, Zou W, Shea LD, Moon JJ, Cancer nanomedicine for combination cancer immunotherapy, Nat. Rev. Mater, 4 (2019) 398–414.

[34]. Xue X, Lindstrom A, Qu H, Li Y, Recent advances on small-molecule nanomedicines for cancer treatment, WIREs Nanomed. Nanobiotechnol, 12 (2019) e1607.

[35]. Xue X, Zhao Y, Dai L, Zhang X, Hao X, Zhang C, Huo S, Liu J, Liu C, Kumar A, Chen W-Q, Zou G, Liang X-J, Spatiotemporal Drug Release Visualized through a Drug Delivery System with Tunable Aggregation-Induced Emission, Adv. Mater, 26 (2014) 712–717. [PubMed: 24129910]

[36]. Xue X, Qu H, Bo R, Zhang D, Zhu Z, Xiang B, Li L, Ricci M, Pan C-X, Lin T-Y, Li Y, A transformable nanoplatform with multiple therapeutic and immunostimulatory properties for treatment of advanced cancers, Biomaterials, 299 (2023) 122145. [PubMed: 37172536]

[37]. Li L, Lindstrom AR, Birkeland AC, Tang M, Lin T-Y, Zhou Y, Xiang B, Xue X, Li Y, Deep tumor-penetrating nano-delivery strategy to improve diagnosis and therapy in patient-derived xenograft (PDX) oral cancer model and patient tissue, Nano Res., 16 (2023) 2927–2937.

[38]. Xue X, Huang Y, Wang X, Wang Z, Carney RP, Li X, Yuan Y, He Y, Lin T.-y., Li Y, Self-indicating, fully active pharmaceutical ingredients nanoparticles (FAPIN) for multimodal imaging guided trimodality cancer therapy, Biomaterials, 161 (2018) 203–215. [PubMed: 29421556]

[39]. Xue X, Huang Y, Bo R, Jia B, Wu H, Yuan Y, Wang Z, Ma Z, Jing D, Xu X, Yu W, Lin T.-y., Li Y, Trojan Horse nanotheranostics with dual transformability and multifunctionality for highly effective cancer treatment, Nat. Commun, 9 (2018) 3653. [PubMed: 30194413]

[40]. Su H, Koo JM, Cui H, One-component nanomedicine J Control. Release, 219 (2015) 383–395.

[41]. Cheetham AG, Chakroun RW, Ma W, Cui H, Self-assembling prodrugs, Chem. Soc. Rev, 46 (2017) 6638–6663. [PubMed: 29019492]

[42]. Cheetham AG, Zhang P, Lin Y.-a., Lock LL, Cui H, Supramolecular Nanostructures Formed by Anticancer Drug Assembly, J. Am. Chem. Soc, 135 (2013) 2907–2910. [PubMed: 23379791]

[43]. Niu RG, Jing H, Chen Z, Xu JP, Dai J, Yan Z, Differentiating malignant colorectal tumor patients from benign colorectal tumor patients by assaying morning urinary arylsulfatase activity, Asia-Pac. J. Clin. Onco, 8 (2012) 362–367.

[44]. Xu J, Xu L, Wang C, Yang R, Zhuang Q, Han X, Dong Z, Zhu W, Peng R, Liu Z, Near-Infrared-Triggered Photodynamic Therapy with Multitasking Upconversion Nanoparticles in Combination with Checkpoint Blockade for Immunotherapy of Colorectal Cancer, ACS Nano, 11 (2017) 4463–4474. [PubMed: 28362496]

[45]. Moghimi SM, Szebeni J, Stealth liposomes and long circulating nanoparticles: critical issues in pharmacokinetics, opsonization and protein-binding properties, Prog. Lipid Res, 42 (2003) 463–478. [PubMed: 14559067]

[46]. Owens DE, Peppas NA, Opsonization, biodistribution, and pharmacokinetics of polymeric nanoparticles, Int. J. Pharm, 307 (2006) 93–102. [PubMed: 16303268]

[47]. Barenholz Y, Doxil® — The first FDA-approved nano-drug: Lessons learned, J. Control. Release, 160 (2012) 117–134. [PubMed: 22484195]

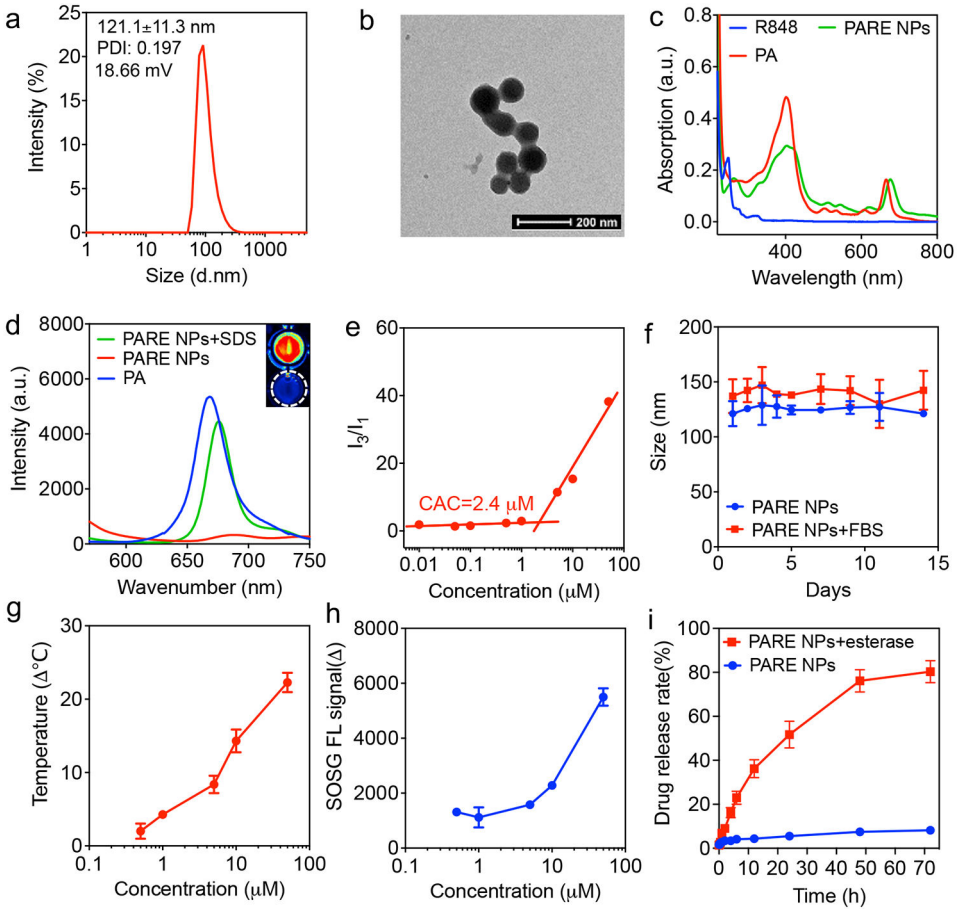

Fig. 1. Characterization of PARE NPs.

a) The particle size, surface charge and polydispersity index (PDI) of PARE NPs (50 μM). b) The transmission electron microscopic (TEM) micrograph of PARE NPs (50 μM). c) UV–vis absorption of PA, R848 and PARE NPs (50 μM). d) Fluorescence spectra of PA, PARE NPs (50 μM) and PARE NPs (50 μM) with 10% SDS. Inset is the near-infrared imaging of PARE NPs in the presence (upper) or absence (lower) of SDS. e) The critical aggregation concentration (CAC) of PARE NPs. f) Stability of PARE NPs (100 μM) with or without 10% fetal bovine serum (FBS). g) Photodynamic effect of PARE NPs indicated by ROS production. h) Photothermal effect of PARE NPs indicated by hyperthermia generation. i) The accumulative drug release of PARE NPs (100 μM) upon esterase hydration.

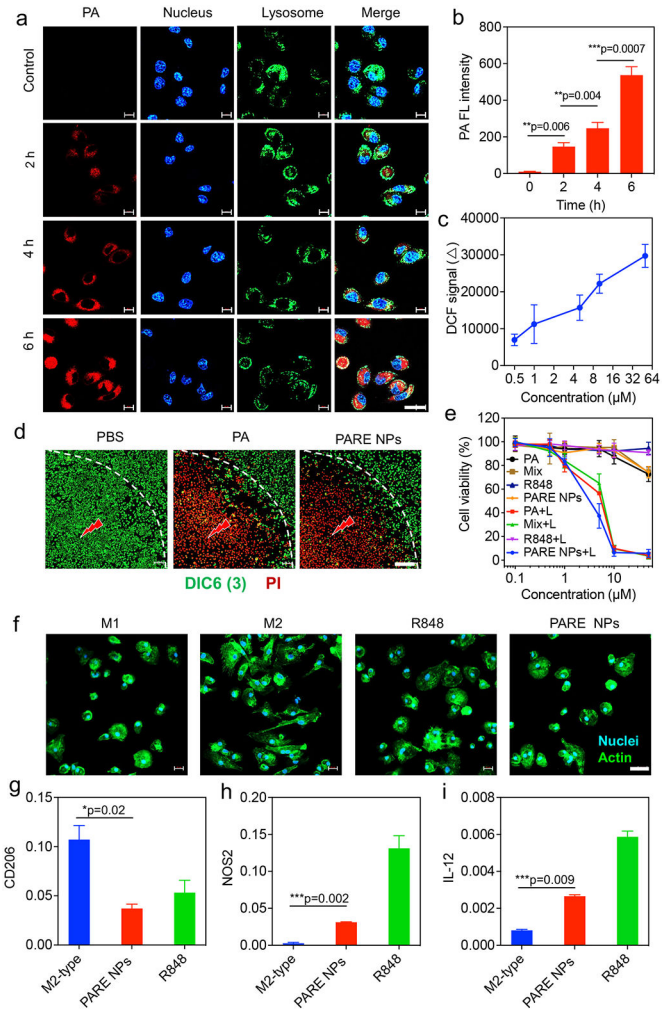

Fig. 2. In vitro cell assays.

a) The uptake of PARE NPs (10 μM) in SCC-7 cells. The scale bar is 40 μm. b) Quantitative analysis of the cell uptake by monitoring the PA fluorescence based on a). c) The intracellular ROS production of PARE NPs in SCC-7 cells. d) The controllability of the PARE NPs' phototherapeutic effect, the red lightening indicates laser-treated area. The live and dead cells were indicated by DIC6(3) and PI, respectively. The scale bar is 200 μm. e) Cell viability of SCC-7 cells treated with various materials. f) The M2 to M1 polarization of BMDMs indicated by morphological analysis. The scale bar is 40 μm. Specific cytokine expressions, including g) CD206, h) NOS2 and i) IL-12 of M1 or M2-like cells analyzed by RT-qPCR.

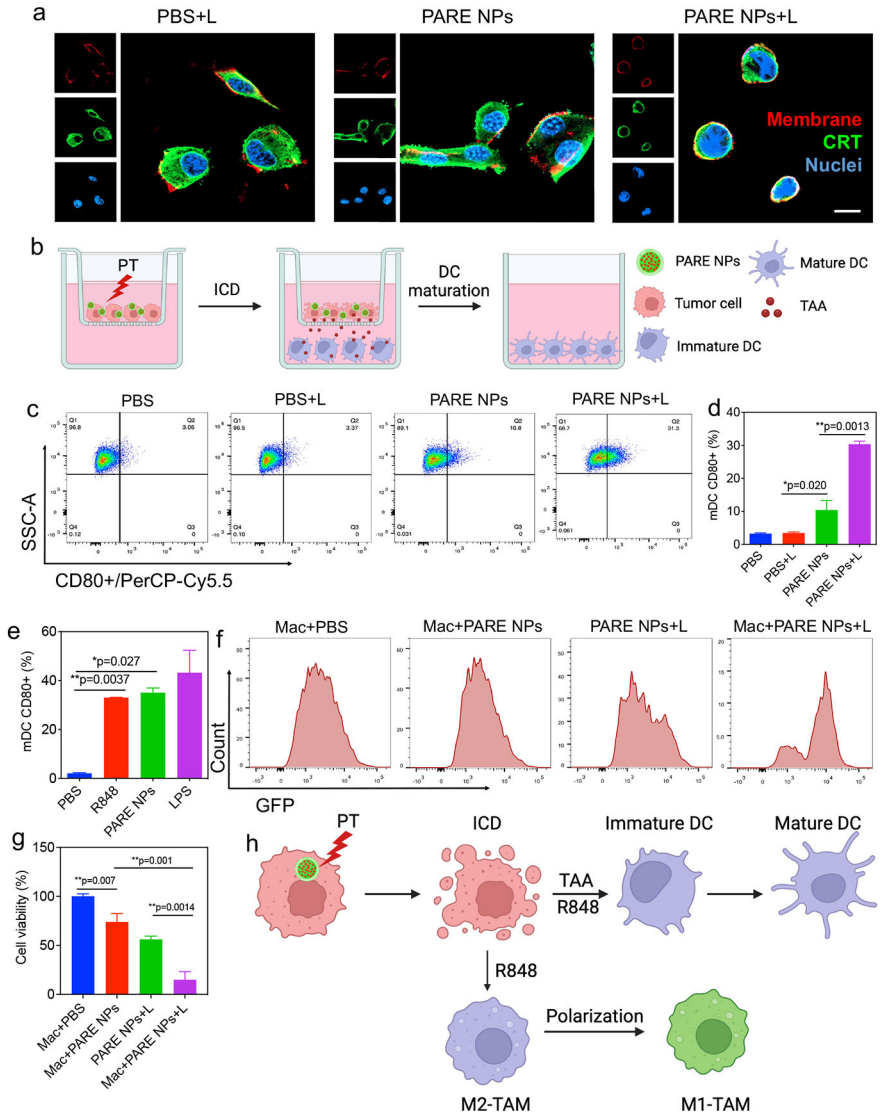

Fig. 3. The phototherapy-promoted immune response of PARE NPs at the cellular level.

a) Calreticulin (CRT) dislocation in PARE NPs-treated SCC-7 cells. The scale bar is 20 μm. b) Schematic diagram depicted the Transwell experiment. c) Flow cytometry results showed the CD80+/Percp-Cy5.5 expression in DC in the Transwell system. d) Quantification of CD80 expression in c). e) The mDC-promoting effect of R848 and PARE NPs. f) The cytotoxicity study of PARE NPs in a co-cultured model of SCC-7/GFP cells and macrophages. g). Quantification of SCC7-GFP cells viability in f). Mac denotes macrophage. h) Schematic diagram illustrated the phototherapy-promoted immunotherapy of PARE NPs.

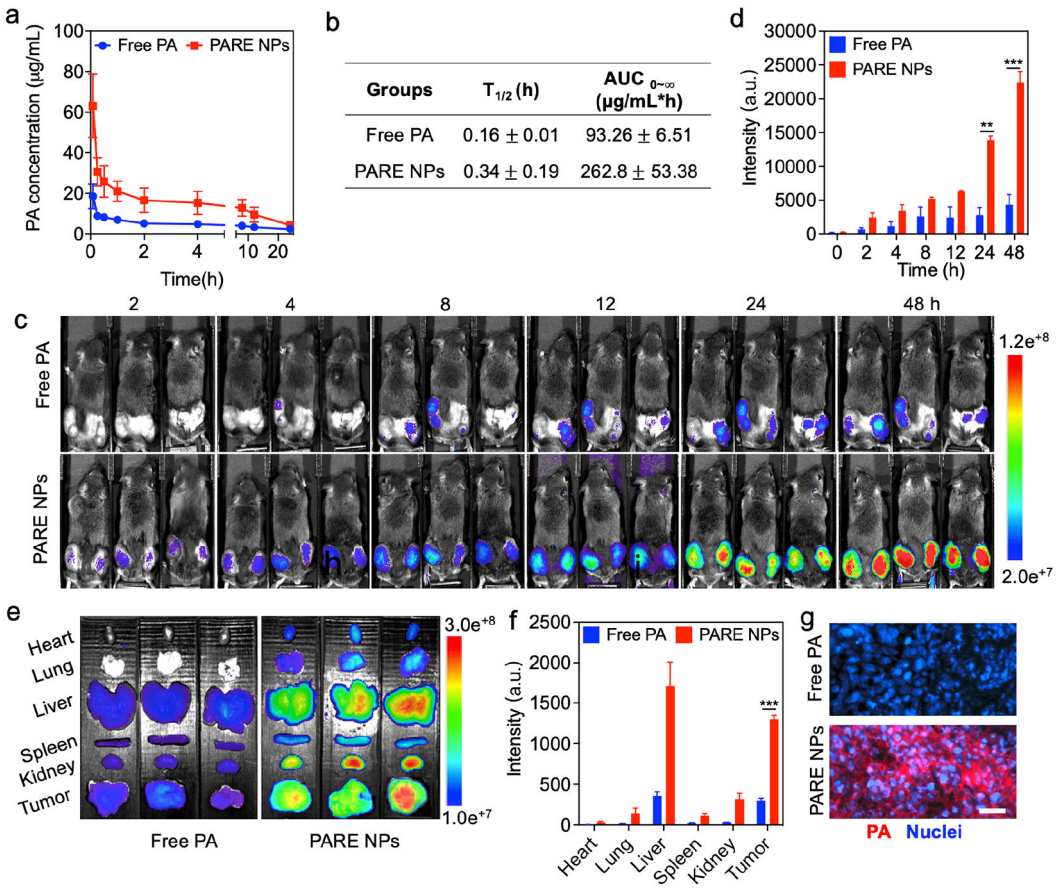

Fig. 4. In vivo performance of PARE NPs.

a) PK profile of PARE NPs. The free PA was employed as a surrogate for free drug control. b) The PK parameters of PARE NPs and free PA. c) NIRF imaging of SCC-7 tumor-bearing mice. d) Quantitative data showed the tumor accumulation of PARE NPs based on c). e) The *ex-vivo* NIRF imaging of major organs and tumors at 48 h post-injection. f) Quantitative data showed the biodistribution of PARE NPs and PA based on e). g) Cryo-section of the tumor tissue in e) showed the tumor infiltration of PARE NPs and PA. The scale bar is 50 μm.

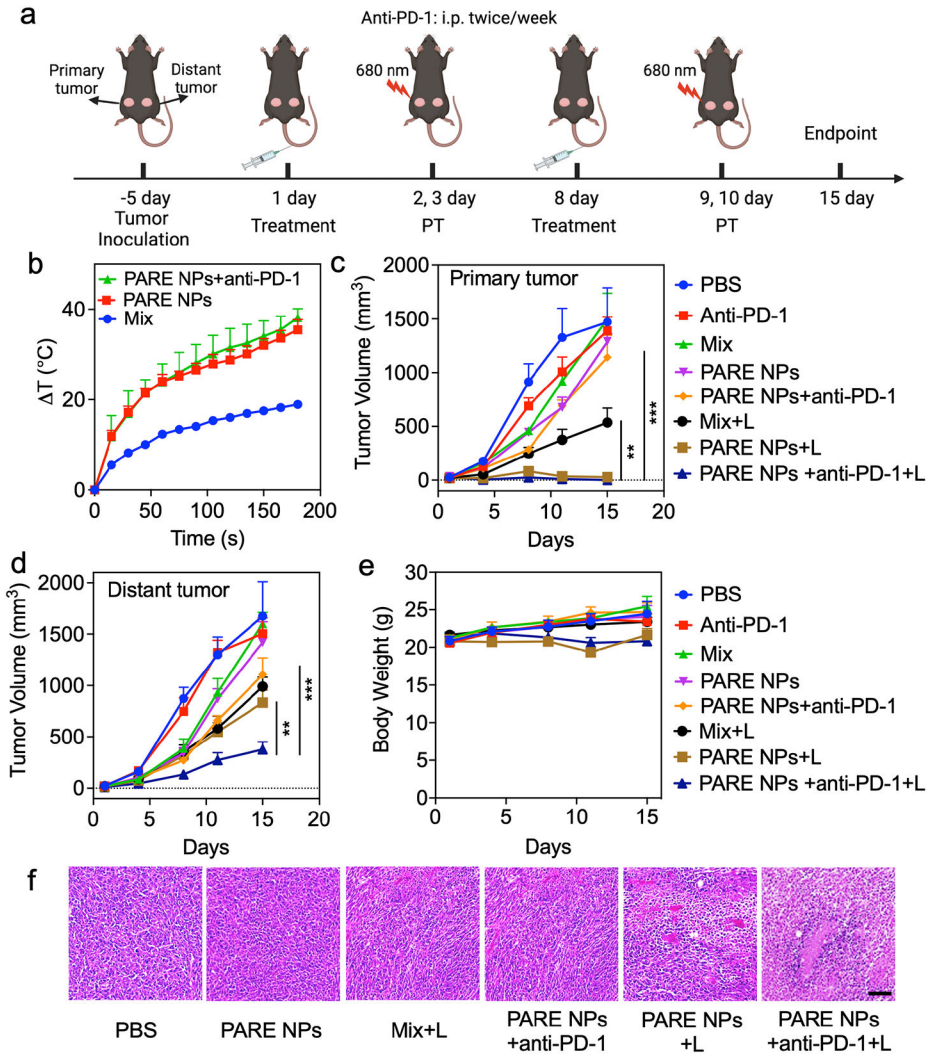

Fig. 5. *In vivo* anti-tumor activities of PARE NPs.

a) The establishment of subcutaneous HNSCC tumor mouse model, and the subsequent animal-treating schedules. The laser (680 nm) dose was set as 0.5 W/cm^2 for 3 min. b) The photo-induced hyperthermia at the tumor site on the Mix+L, PARE NPs +L and PARE NPs+anti-PD-1+L treated mice. c) The tumor volume changes of primary tumors. d). The tumor volume changes of distant tumors. e) Body weight changes of tumor-bearing mice. f) H&E stain of the tumor tissue. The scale bar is 100 μm.

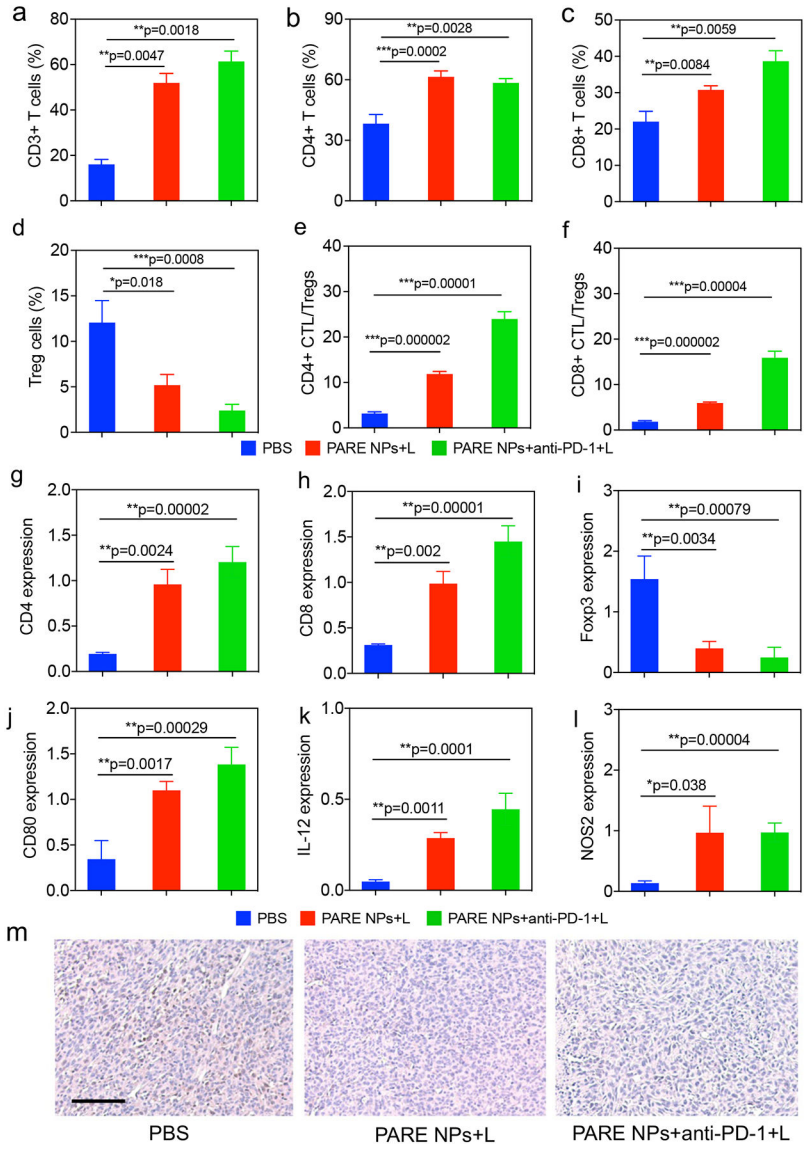

Fig. 6. The mechanism of the phototherapy-promoted immunotherapy.

FACS results showed the percentage of a) CD3+ T cells, b) CD4+ T cells, c) CD8+ T cells and d) Tregs in distant tumors. The ratios of e) CD4+ CTL/Tregs and f) CD8+ CTL/Tregs. The expression of g) CD4, h) CD8 and i) Foxp3 were evaluated by RT-qPCR. RT-PCR showed the expression of j) CD80, k) IL-12, and l) NOS2 in different groups. n=5, 5 out 8 mice were randomly taken for FACS and RT-qPCR analysis. m) IHC results showed the Ki67 expression in different groups. The scale bar is 100 μm.

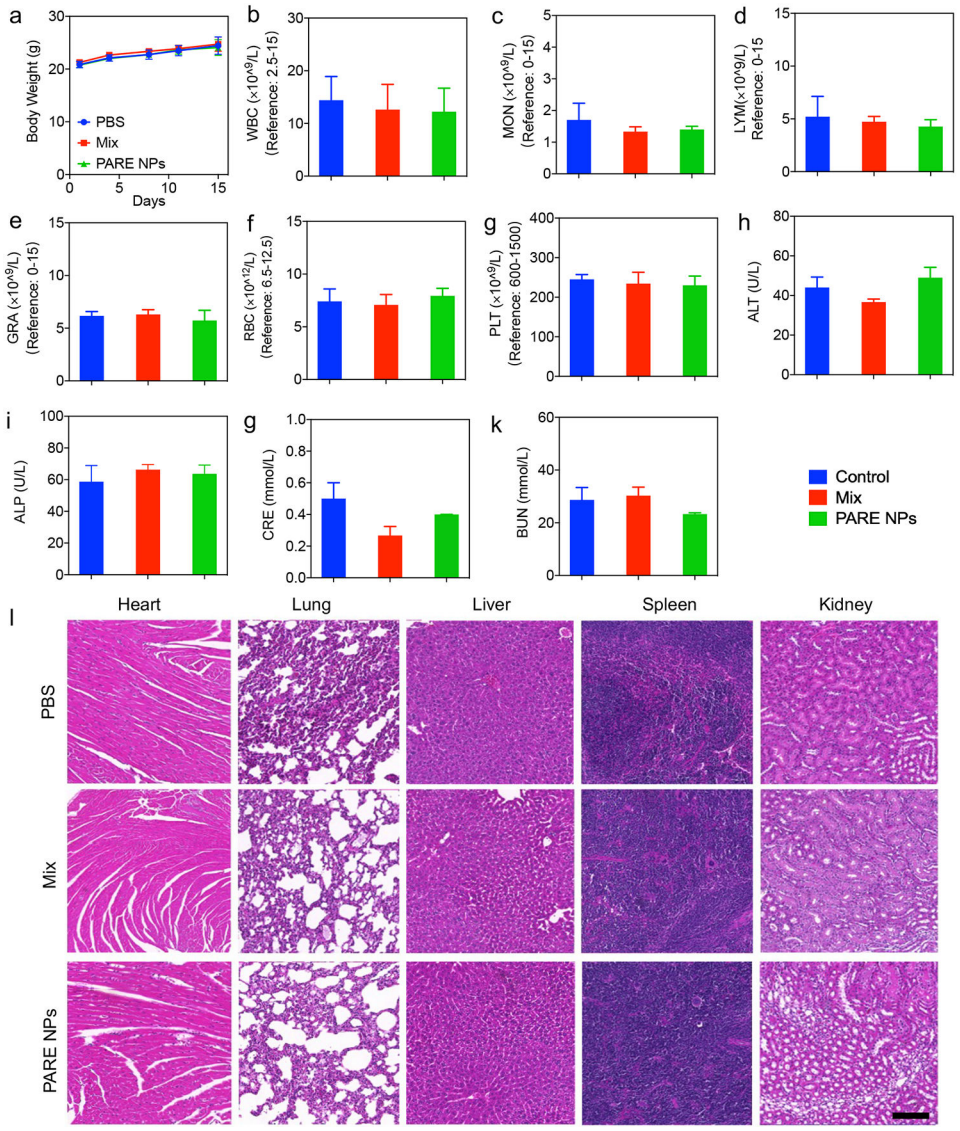

Fig. 7. Biocompatibility of PARE NPs.

a) The body weight changes of the healthy mice treated with PARE NPs and the control materials. b-k) Comparative analysis of hematological parameters. Acronyms: WBC-white blood cell, MON-monocyte, LYM-lymphocyte, GRA-granulocyte, RBC-red blood cell, PLT-platelet. Liver function parameters: ALT-alanine transaminase, ALP-alkaline phosphatase. Kidney function parameters: CRE-creatinine, BUN-blood urea nitrogen. l) The comparison of main organ histopathology. The scale bar is 100 μm.

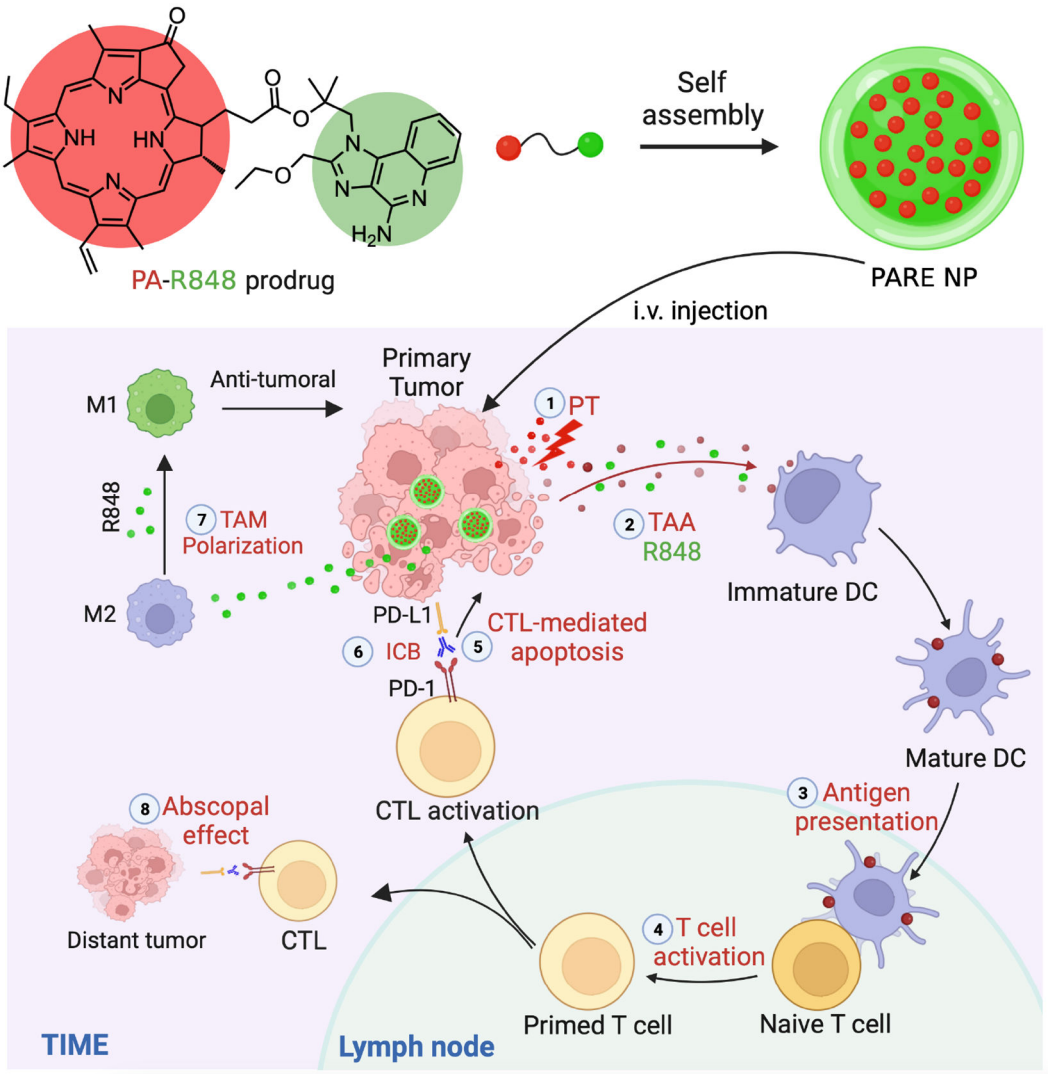

Scheme 1. Schematic illustration showed the self-assembly of PARE NPs and their photo-/immune- therapies for the synergistic treatments of primary and distant tumors.